

NUMERICAL MODELING OF HORIZONTAL ANNULAR FLOWS USING A DROPLET ENTRAINMENT MODEL

T. Höhne

Helmholtz-Zentrum Dresden-Rossendorf (HZDR) - Institute of Fluid Dynamics
P.O.Box 510119,
D-01314 Dresden, Germany
t.hoehne@hzdr.de

Abstract

One limitation in current simulating horizontal annular flows is the lack of treatment of droplet formation mechanisms. For self-generating annular flows in horizontal pipes, the interfacial momentum exchange and the turbulence parameters have to be modelled correctly. Furthermore the understanding of the mechanism of droplet entrainment in annular flow regimes for heat and mass transfer processes is of great importance in the chemical and nuclear industry.

A new entrainment model within the AIAD framework is proposed. It assumes that due to liquid turbulence the interface gets rough and wavy and forms droplets. The new approach is validated with HZDR annular flow experiments. Important phenomena like the pressure drop, the wave pumping effect, the droplet entrainment, the liquid film formation and the transient flow behavior could be calculated, analyzed and some of the phenomena compared with the measurement.

Keywords: CFD, horizontal annular flow, AIAD, droplet entrainment, two-phase flow

1. Introduction

Annular flow occurs in many industrial processes, and is characterized by high gas flow at the center of the pipe and liquid film flow around the pipe wall. Due to the high gas velocity, large shear velocities are induced that result in high interfacial shear stress causing continuous entrainment of liquid droplets into the gas core from the liquid film. When the liquid fraction is small in horizontal annular flow, it is possible to cause an extremely important problem that relates to the damage of heat exchanger tubes, because the drainage of liquid due to gravity, as well as the evaporation, leads to the dry-out of thin liquid film near the top of the tube. Therefore, it is important to accurately predict the circumferential distribution of film thickness in horizontal annular flow. Furthermore the thin water film at the cold wall plays a major role for the heat transfer resistance of the condensation process. For better understanding of condensation heat transfer the film formation mechanism and the film distribution need to be known.

Since many years, measurements of the wave structure of the liquid film have been made for both, vertical and horizontal annular flows. These measurements included local time variation of film thickness, wave velocity, and frequency, as well as spectral properties of film thickness time records. In these studies, resistance probes (Jayanti et al. 1990 and Paras and Karabelas 1991) and optical methods were employed (Shedd and Newell 1998). More recently, Koplín (2004) obtained partial success with particle image velocimetry (PIV) and particle tracking techniques to estimate velocity field in the film.

Today's theories to explain the annular flow mechanism are wave spreading, wave pumping, secondary gas flow and entrainment of droplets into the waves.

The *Wave Spreading* mechanism was described by Buttsworth and Pulling (1972) and Fukano and Ousaka (1989). They assume that disturbance waves travel faster along the bottom than along the top, creating a plowing or wedge effect that pushes the liquid film upwards in front of the wave and keeps the liquid film on top.

A *Wave Pumping* Mechanism was proposed by Fukano and Ousaka (1989) and first shown by Darling and McManus (1968). Later, also Paras et al. (1991) did analyze the Wave Pumping Mechanism. They found out that waves travel upward due to circumferential pressure gradients and liquid drains by gravity after the passage of each wave. The authors further suggest that the circumferential pressure gradient is caused by stagnation of gas in front of the disturbance wave and the separation behind it, which is higher on the bottom part than on top.

The *Secondary Gas Flow* was first proposed by Pletcher and McManus (1965) and shown by Darling and McManus (1968). Later, also Paras et al. (1991) observed this gas flow structure. The motion is caused by interfacial roughness circumferential gradient. According to Flores et al. (1995), secondary flow velocity is about 4% of axial velocity. Westende et al. (2007) compared the behaviour of the droplets (dispersed phase) with and without secondary flow, using LES. It was shown that the presence of secondary flow increases the droplet concentration in the core of the pipe and the droplet deposition-rate at the top of the pipe.

Droplet Entrainment/Deposition: Azzopardi (1980) found that droplets in annular core come predominantly from the surface of disturbance waves. Stevanovic and Studovic (1995) presented a derivation for droplet entrainment in vertical annular flow, it is extensively used for all configurations. Kopplin (2004) suggests that this mechanism becomes more important as the flow goes further into the annular regime. Entrainment fraction results from a dynamic equilibrium between the rate of deposition of drops from the gas core to the liquid film and the rate of droplet formation (also called atomization) at the gas-liquid interface from waves occurring on the film surface. Its prediction is important for the estimation of pressure drop, flow rate, liquid holdup, dry-out in annular flow as well as for designing and optimizing separation facilities. It should be noted that the phenomenon of dry-out, also known as Critical Heat Flux (CHF), corresponds to the point where a continuous liquid contact cannot be maintained at the surface. This has importance in the nuclear industry since droplet entrainment and deposition rates need to be known to predict dry-out. According to Kataoka and Ishii (1982), the entrainment fraction is a more stable parameter to measure and correlate as this represents the integral effects of deposition and entrainment rate of the droplets.

In general, the conditions leading to entrainment of a liquid surface film by a gas flow is of considerable practical importance for heat and mass transfer processes in two-phase flow systems. The mechanisms of mass, momentum, and energy transfer is significantly altered by the inception of entrainment (Ishii et al., 1975). A wavy liquid surface can be entrained into a gas flow in different ways. Hydrodynamic and surface forces govern the motion and deformation of the wave crests. Under certain conditions, these forces lead to an extreme deformation of the interface which results in breakup of a portion of a wave into several droplets. The forces acting on the wave crests depend on the flow pattern around them as well as on the shape of the interface. Ishii et al. explained in his paper five basic types of entrainment mechanisms, while four of them are relevant in segregated horizontal flow regimes which are shown in Fig. 1. In the first type the tops of large amplitude roll waves are sheared off from the wave crests by the turbulent gas

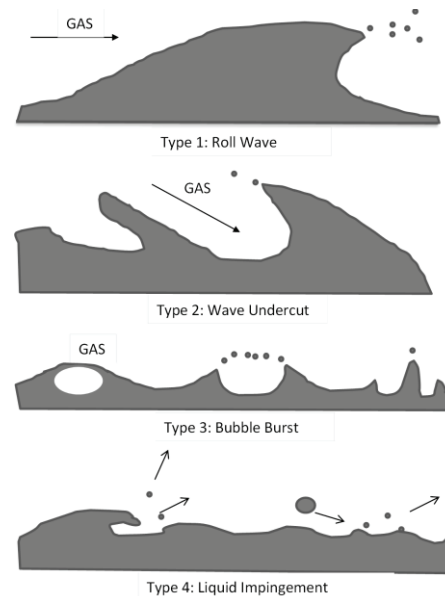


Fig. 1 Different droplet entrainment mechanisms (Ishii, 1975)

flow (Hewitt and Hall-Taylor, 1970). The drag force acting on the wave tops deforms the interface against the retaining force of the liquid surface tension. The second type of entrainment is caused by undercutting the liquid film by a gas flow (Hewitt and Hall-Taylor, 1970). The third type is related to the bursting of gas bubbles. It was shown in Hewitt (1954) that drops can be generated by a bubble rising to the surface of a liquid. The fourth type of entrainment is caused by the impinging of the liquid drops or mass to the film interface. Advancing roll-wave fronts may produce small size droplets by this mechanism. A universal droplet entrainment model should cover all these cases. In general, there should be no problem to model these types of entrainment. More effort in the future has to be done to describe bubble bursting (type 3) and impinging of the liquid drops (type 4).

2. Algebraic Interfacial Area Density Model

The development of general computational fluid dynamics (CFD) models, which are closer to physics and include less empiricism, is a long-term objective of the activities of the Helmholtz-Zentrum Dresden-Rossendorf (HZDR) research programs. Such models are an essential precondition for the application of CFD codes to the modelling of flow related phenomena in the chemical and nuclear industries. The new formulation for the interfacial drag at the free surface and turbulence parameters within the algebraic interfacial area density model (AIAD) is one result of these HZDR activities (Höhne and Mehlhoop, 2014). The AIAD approach allows the use of different physical models depending on the local morphology inside a macro-scale multi-fluid framework. A further step of improvement of modelling interfaces is the consideration of droplet entrainment mechanisms.

The AIAD model was developed in close cooperation by ANSYS and HZDR and is described in more detail in Yegorov (2004) and Höhne and Mehlhoop (2014).

The basic idea of the model is:

- The interfacial area density (IAD) allows the detection of the morphological form and the corresponding switch of each correlation from one object pair to another.
- It provides a law for the interfacial area density and the drag coefficient for a full range of phase volume fractions from no liquid to no gas.
- The model improves the physical modelling in the asymptotic limits of bubbly and droplet flows.
- The interfacial area density in the intermediate range is set to the interfacial area density for free surface.

The approach used in the AIAD model is to define blending functions depending on the volume fraction that enable switching between the morphologies of dispersed droplets, dispersed bubbles and the free surface. Based on these blending functions, different equations for the interfacial area density and the drag coefficient can be applied according to the local morphology. The blending functions are defined as Eq. (1) and Eq. (2) for droplet and bubble region, respectively and Eq. (3) for the free surface:

$$f_D = [1 + e^{a_D(\alpha_L - \alpha_{D,limit})}]^{-1} \quad (1)$$

$$f_B = [1 + e^{a_B(\alpha_G - \alpha_{B,limit})}]^{-1} \quad (2)$$

$$f_{FS} = 1 - f_D - f_B \quad (3)$$

with α_L is the volume fraction of the liquid phase, α_G the volume fraction of the gas phase, a_D and a_B being the blending coefficients for droplets and bubbles, respectively and $\alpha_{D,limit}$ and $\alpha_{B,limit}$ the volume fraction limiters. In the simulations presented here, values of $a_D = a_B = 70$ and $\alpha_{D,limit} = \alpha_{B,limit} = 0.3$ were used. For all model coefficients same values were used as in previous studies (Höhne et. al 2010, 2011 and 2014). They were chosen independent of the actual geometry and flow regime and no tuning of the AIAD model was done for the work presented here. The threshold value $\alpha_{B,limit} = 0.3$ is a critical volume fraction before the coalescence rate increases sharply and is verified by

experiments in both vertical and horizontal flows. Parameter studies also indicated that the model is not very sensitive towards a change of the blending function parameters.

For simplicity bubbles and droplets are for now assumed to be of spherical shape, with a constant diameter of d_B and d_D , respectively. The resulting formulation for the interfacial area density for droplets, A_D , is given by

$$A_D = \frac{6\alpha_L}{d_D}. \quad (4)$$

The IAD for bubbles, A_B , is formulated analogous. The IAD of the free surface, A_{FS} , is defined as the magnitude of the gradient of the liquid volume fraction α_L , as given in Eq. (5), with \mathbf{n} being the normal vector of the free surface.

$$A_{FS} = |\nabla\alpha_L| = \frac{\partial\alpha_L}{\partial n} \quad (5)$$

The local interfacial area density A is then calculated as the sum of A_j , weighted by the blending functions f_j :

$$A = \sum_j f_j A_j, \quad j = FS, B, D \quad (6)$$

3. The entrainment model

Moraga et al. (2008) developed a 3-D two-fluid model which is capable of simulating bubbly flows around surface ships. A sub-grid model was developed to determine the bubble source due to air ingestion. This model was based on the simple observation that the non-linear dependence of the terminal velocity with bubble diameter creates a region of high void fraction in and around the air entrainment region. Also Ma et al. (2011) described a model for the air entrainment. He calculated the position of the surface using a single-phase level-set function. Later on in a second step the entrainment is calculated as a volume source using the two-fluid model.

Using some of the ideas of the air entrainment models of Moraga et al. (2008) and Ma et a. (2011) assumptions have to be made to find a universal droplet entrainment model. The proposed entrainment model assumes that due to liquid turbulence the interface gets rough and wavy and forms bulbs with an average size of $a(x)$ (see Fig. 2). All droplet formations occur in a layer close to the interface, which has a thickness of $C_1 a$ (C_1 is a non-dimensional constant parameter). The rate of droplet formation is estimated by the quantity of liquid passing an interfacial layer relative to the velocity of the interface. Consequently, the liquid film is forming a droplet only if the water bulb moves upward into the gas phase relative to the interface. The roughness is estimated in Fig. 2 as $a = C_2 k/g$ (C_2 is a non-dimensional constant parameter) with $k(x)$ being the local liquid turbulent kinetic energy including the sub-grid wave turbulence [see Höhne and Mehlhoop (2014)] since it has an influence on the surface turbulence budget.

With the assumptions of Fig. 2 this leads to a local deposition rate:

$$d(x) = \frac{C_{Drop}}{g} k(x) \frac{\partial u_n}{\partial n}(x) \quad (7)$$

with $C_{Drop} = C_1 C_2$ as a new constant. The parameter C_{Drop} is left undetermined and should depend on the fluid pair properties. The created droplets are then distributed as a volume source at the interface in a layer, which is ϕ_{Drop} thick.

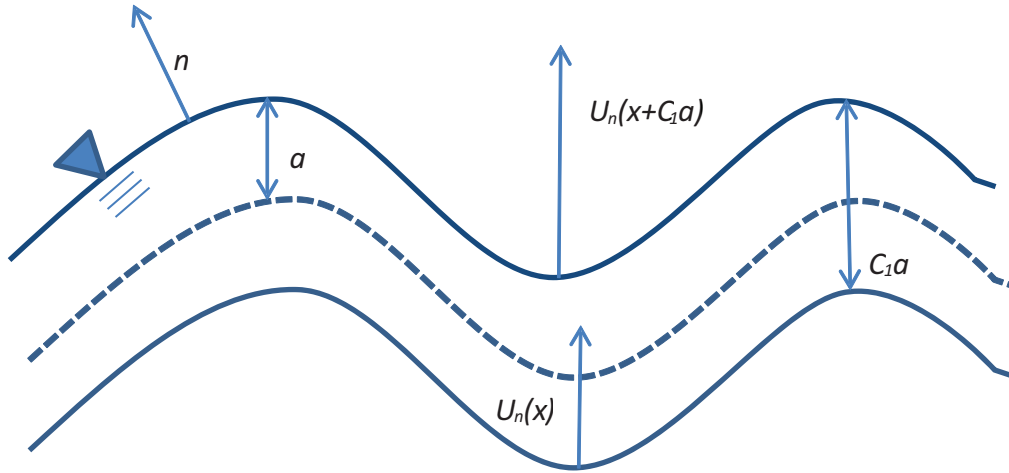


Fig. 2 Schematic diagram of droplet entrainment

Therefore, the droplet formation rate per unit volume and time is:

$$D(x) = \frac{C_{Drop}}{g\phi_{Drop}} k(x) \frac{\partial u_n}{\partial n}(x) \quad (8)$$

The rate (Eq. 8) is essentially determined by two local key variables: the turbulent kinetic energy and the outward velocity gradient. On the other hand if droplets occur below the water surface a complete coalescence should lead to a mass transfer of the droplets into the continuous liquid phase. This is prescribed in the following continuity source/sink term:

$$\dot{m}_{dl \rightarrow cl}(x) = f_B \cdot \alpha_{Drop} \cdot \rho_{liq} / \Delta t \quad (9)$$

While the model of Ma et al. (2011) is assuming the formation process occurring in a thin layer underneath the free surface, in our case this layer is supposed to be the thickness of smeared interface, that we defined to be $\Delta_{Drop} = C_1 a = 4 \Delta x$ (grid size dependent) similar to the GENTOP concept in Hänsch et al. (2012).

In the AIAD framework the 3rd phase “droplet” is added to the gas and the liquid phase to form a three-phase flow. The material properties are taken from the liquid phase and a uniform mean droplet diameter is assumed. This droplet phase will be activated within the detected free surface region using the function f_{FS} . The mass of the droplet phase is defined as a continuity source for dispersed water respectively sinks for the continuous water in the form of:

$$m_{Drop}(x) = f_{FS} \rho_l \alpha_l D(x) \quad (10)$$

$$D_{Drop}(x) = \frac{C_{Drop}}{4\Delta x g} k_l(x) \frac{\partial u_{l,n}}{\partial n}(x) \quad (11)$$

The parameter C_2 is left undetermined and is set to 0.01 in present simulations (similar to Hänsch 2012). It should depend on the fluid pair properties.

4. The experiment

Based on generic studies on high pressure condensation at the thermo hydraulic test facility TOPFLOW (HZDR) experiments concerning the defined generation of annular flow in a tube with small diameter were performed. The results were used for a comparison toward CFD calculations and for the characterization of local phenomena. The test rig was developed for steam water flows, but for CFD validation an experiment with air/water was chosen to separate condensation effects.

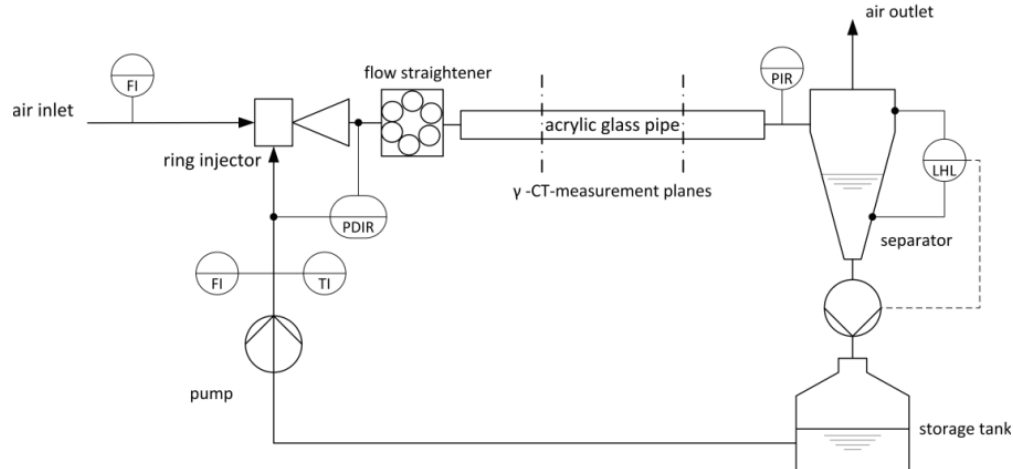


Fig. 3 Schematic experimental setup and peripherals.

The test section consist of an acrylic glass pipe with an inner diameter of 43,3 mm and a length of 1500 mm. The pipe has an inclination of approximately 0.7°. The schematic of test section and the required peripherals are shown in Fig. 3.

The annular flow is generated by a ring injector. A ring chamber around the core gas flow provides water into the pipe. This principle ensures the presence of an annular flow from the beginning of the two phase flow. A vortex in the water film caused by the injection geometry is removed by a flow straightener. Behind the test section the two phase mixture is separated in a hydro cyclone. The volume flow rates of air and water, the inlet temperature and the pressure difference are measured simultaneously. The experiments were conducted at atmospheric pressure and room temperature.

The experiments were conducted in the operating area of the ring injector, therefore the water volume flow rates were $\dot{V}_{water} = 0,4 L/s \dots 0,8 L/s$ and the air volume flow rates were $\dot{V}_{air} = 100 Nm^3/h, 150 Nm^3/h, 200 Nm^3/h$. The investigated experimental conditions are shown in the flow regime map by Taitel and Dukler (1976) in Fig 4. All of the matrix points can be found in the region of annular flow as expected.

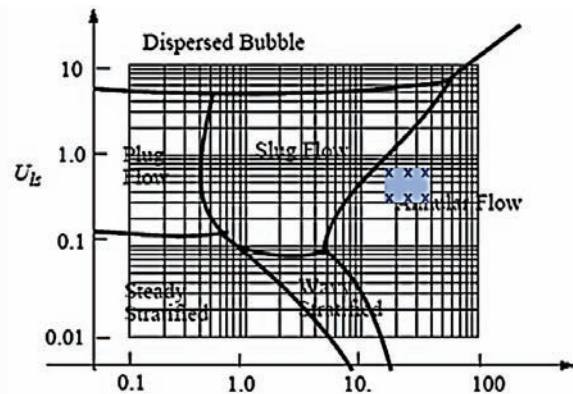


Fig. 4 Flow regime map from Taitel and Dukler (1976) for horizontal annular flow with experimental points

The measurements of the flow structure were performed at 291 mm and 817 mm behind the tube inlet (Fig. 8) due to requirements of the application of the injection system. The given dimensions correspondent to aspect ratios of 6,7 L/D and 18,9 L/D.

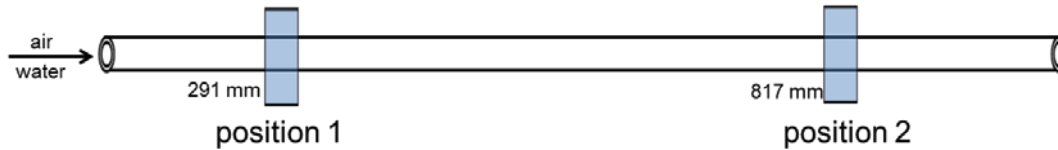


Fig. 5 Measurement position of the gamma ray tomography.

As it is shown in Fig. 6a the detailed flow structure cannot be resolved by optical observation from outside the tube. Only the principle wavy structure of the water film can be divined. To achieve the desired results non-invasive measurement technique with high resolution has to be applied.

For such investigations, a gamma-ray computed tomograph called CompaCT was developed by Bieberle et al. (2013). The installed CompaCT onto the acrylic glass pipe is shown in Fig. 6 b.

The CompaCT system consist of a collimated ^{137}Cs source (photon energy: ≈ 662 keV, activity: 1,1 GBq) oppositely directed to an in-house developed gamma-ray detector arc. The detector arc comprises 112 scintillation detector elements, each with an active area of 4 mm in height and 2 mm in width. Thus, the in-plane resolution was determined to approximately 2-3 mm. The detectors are operated in pulse mode, thus, scattered photon can be excluded from measurements by making only the photo peak area of the used source in the spectrum. Furthermore, the measurement system is thermally stabilised by what high repeating measurement accuracy is achieved for wide ambient temperature fluctuations. The distance between the source and the detector arc is approximately 260 mm. Together with a radiation angle of 60° a region of interest of up to a diameter of 130 mm can be investigated.

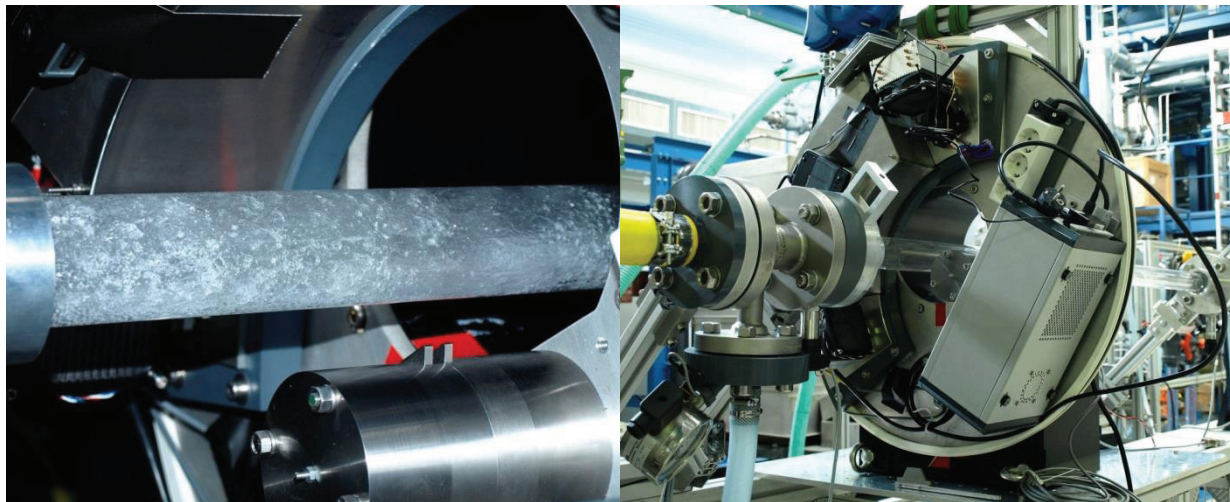


Fig. 6 a. Visual impression of the annular flow experiment. b. Gamma-ray tomograph mounted in the test facility.

For a full CT scan the source detector arrangement is rotated 360° around the object and the attenuation of radiation in correlation to the turning angle is measured. By using the well-known computer tomography reconstruction algorithm “filtered back projection” cross sectional material distributions of the scanned object can be obtained, without interfering the internal process. The measuring time was determined to 20 min for one complete scan that was determined in preliminary studies at typical annular flow material distributions as an optimum between measuring time and measuring accuracy. This leads to cross sectional images containing a time averaged flow structures of the inner section of the pipe.

The experimental set up and the used measurement techniques allow the determination of the film thickness distribution, the pressure drop over the test section and can give an idea about the wave behavior. The cross sectional images together with the operation data can be used as comparison data with CFD calculation.

5. Numerical setup

A mesh with hexahedral cells was used. The AIAD model and the droplet entrainment model were implemented into the commercial CFD code ANSYS CFX 14.5 by CFX Command Language (CCL). The data for the comparison with the experiments were taken at the measurement positions. To generate appropriate inlet boundary conditions, turbulent velocity profiles were taken. As outlet boundary condition a constant pressure outlet was defined, with the volume fraction function and the hydrostatic pressure also used for the initial conditions. The initial state was an empty pipe with no gas or liquid velocities. The droplet phase was set to zero at the beginning.

The small pipe inclination of the experiment was neglected in this study, since it is very low. The simulation was run in transient mode. In a grid study three meshes were compared. For the coarsest mesh 1 (40000 nodes) convergence was not achieved. For mesh 2 (470000) and mesh 3 (3 Mio.) the profiles of the velocity in main flow direction were analyzed and showed no qualitative difference between the profiles and the quantitative deviation was sufficiently small. The maximum difference was less than 1%. For further calculations the mesh 2 was used, since it showed good convergence behavior during an acceptable CPU time period.

An Euler-Euler multiphase model using fluid dependent RANS turbulence models was applied (ANSYS CFX, 2013). The high-resolution discretization scheme was used for convection terms in the equations. For time integration, the fully implicit second order backward Euler method was applied with a constant time step of $\Delta t = 0.001$ s and a maximum of 15 coefficient loops per time step. Convergence was defined in terms of the RMS values of the residuals, which was less than 10^{-4} .

6. Results

A liquid film and droplet spreading could be observed in the simulations. A strong transient behaviour of the flow field is seen in Fig. 7 and Fig. 8. The liquid (dark blue iso-surface 0.5) and droplet volume fraction (light blue iso-surface 0.5) distribution on the pipe wall (0.5s and 0.6s after start of simulation) were selected to show the liquid film and droplet spreading behaviour in the pipe during the annular flow regime. Fig. 7 and Fig. 8 indicate that most of the constant film exists at the bottom of the pipe. The droplets are distributed in all circumferential directions with changing flow pattern over time. It has been shown that the droplets do not form from the entire liquid film, but rather from the disturbance waves [Cousins and Hewitt (1968), Woodmansee and Hanratty (1969), and Azzopardi and Whalley (1980)].

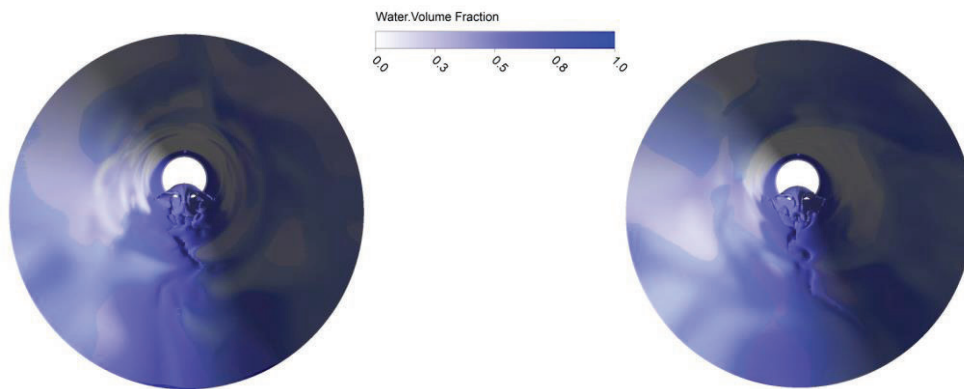


Fig. 7 Liquid and droplet volume fraction (light blue isosurface 0.5) distribution on the pipe wall (0.5s after start of simulation).

Fig. 8 Liquid volume fraction distribution on the pipe wall (0.6s after start of simulation).

It was first suggested by Russell and Lamb (1965) that these droplets, when deposited onto the top of the tube, could maintain the liquid film around the circumference. Almost all wall regions are covered with a liquid film. Wave spreading mechanisms can be observed when comparing the two pictures. The wave spreading theory is based on the idea that the disturbance waves travel faster along the bottom of the tube than along the top. This is thought to create a plowing or wedge effect that pushes liquid film upward immediately in front of the wave. The liquid film thickness can be analyzed using the averaged liquid volume fraction near the wall.

When comparing the experimental results in the Fig. 9 and Fig. 10 with the simulation at the measurement planes 1 and 2 the following conclusions can be made: At the measurement position 1 (Fig. 9, see also Fig. 5) the time averaged liquid volume fraction in experiment and in the simulation is concentrated at the bottom of the pipe with a half-moon shaped form in the experiment and a mushroom shape form in the simulation. Closer observation of the simulations indicated that this shape is created when the two sidewall liquid jets merge and two counter vortices are developing. It is assumed that in the experiment a similar process with the observed shape takes place. In the measurement position 2 (Fig. 10) the time averaged liquid volume fraction in the experiment and the simulation is still concentrated at the bottom of the pipe with a smoother shape. The liquid film in circumferential directions is less than in measurement plane 1 in the experiment and also in the simulation. The averaged liquid film thickness is hard to extract from the measurements. In the simulation the time averaged liquid film thickness at the measurement position 2 amounts at the bottom is 0.5 – 0.8 mm and at the top 0.2 mm. The liquid film is thickest on the bottom of the tube, thinner on the sides of the tube, and the thinnest on the top.

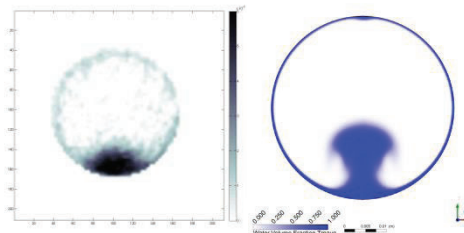


Fig. 9 Comparison of averaged liquid volume fraction at measurement position 1 (experiment, CFX).

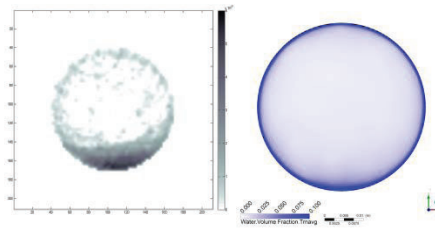


Fig. 10 Comparison of averaged liquid volume fraction at measurement position 2 (experiment, CFX).

The variation in film thickness, along with the disturbance waves, produces an interfacial roughness gradient around the circumference of the tube. This gradient produces a secondary flow normal to the tube axis. Moreover at the top part of the pipe additional secondary flow effects are noticeable.

The pressure drop is strongly dependent on the water film thickness and void fractions. The differential pressure was measured and averaged over time and was about $\Delta p = 0.076$ bar, the calculated pressure drop was averaged over 2 s and was $\Delta p = 0.062$ bar, which is 22% lower than in the experiment.

The droplet entrainment rate could not be measured in the current experimental setup. It was calculated and shown in Fig. 11. The time averaged droplet entrainment rate is 1.09×10^{-2} [kg/ m³s], the averaged complete coalescence rate is a lot lower at 1.58×10^{-3} [kg/ m³s], which means droplets are transported towards the outlet and do not coalesce with the liquid film. The transient behavior of the droplet entrainment rate and complete coalescence rate during 1s in the pipe in Fig. 11 illustrates the instantaneous wavy formation mechanism. In general, more droplets are formed in the total pipe volume than coalesce. It is assumed, that during the generation of disturbance waves these droplets are formed and transported towards the outlet of the test section. It has been shown already by Cousins and Hewitt (1968) that the droplets do not form from the entire liquid film, but rather from the disturbance waves.

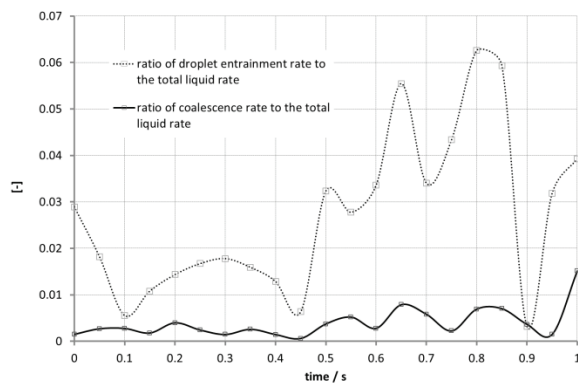


Fig. 11 Droplet entrainment rate and complete coalescence rate to the total liquid rate during 1s.

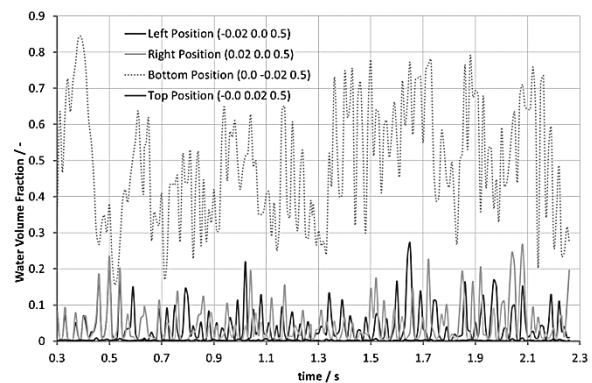


Fig. 12 Mid position of the pipe segment at 0.5 m.

Four analysis points (top, bottom, left and right) for each axial position of the pipe were extracted. Fig.12 shows the transient liquid volume fraction at these positions at the mid position of the pipe segment at 0.5 m. It is noticeable that still a larger fraction of the liquid exists at the bottom of the pipe. In the diagram small ripples and bigger disturbance waves are observed.

To further analyze the transient flow behavior a fast Fourier transform (FFT) analysis of the liquid volume fraction time data was made and compared with literature data. In Schubring and Shedd (2008) a formulation of the disturbance wave frequency is given.

$$f_{ss} = 0.005 \frac{U_{sg}}{D\sqrt{x}} \quad (12)$$

a characteristic frequency of $f_{ss} = 17.95$ Hz was calculated.

The power spectral density (PSD), which describes how the power of a signal or time series is distributed over different frequencies is used. The strongest signals are due to disturbance waves at lower frequencies. It can be concluded that a characteristic frequency could exist in the range of 10- 20 Hz as it is the second peak frequency.

Summary and Outlook

The understanding of the mechanisms lead to annular flow regime is extremely important for heat and mass transfer in the chemical and nuclear industry. In the literature there are four basic types of annular flow mechanisms which are important. These basic types could be confirmed with a numerical simulation using the AIAD framework including a new droplet entrainment model. An annular flow experiment done at HZDR was used for validation purposes. Important phenomena like the pressure drop, the wave pumping effect, the droplet entrainment rate, the liquid film formation and the transient flow behavior could be calculated, analyzed and some of the phenomena compared with the measurement. Verification and Validation is going on – more experimental data are required for the validation. In future the transient ultrafast electron beam X-ray tomography system "ROFEX" will detect droplet inception and the liquid film behavior.

Acknowledgment

The author thanks the HZDR experimental team Thomas Geissler, André Bieberle and Uwe Hampel for providing the data.

Nomenclature

A	interfacial area density (1/m)
a	surface roughness (m)
α	volume fraction (-)
C	constant (-)
C_D	drag coefficient (-)
d	local deposition rate (m/s)
d	diameter (m)
D	droplet formation rate per unit volume and time (1/s)
f	blending function (-)
f	frequency (Hz)
Φ	interface layer (m)
g	constant of gravity acceleration (m/s^2)
k	turbulent kinetic energy (m^2/s^2)
\mathbf{n}	normal vector of the interface (-)
P	pressure (Pa)
t	time (s)
u	velocity (m/s)
U	characteristic velocity (m/s)
\dot{V}	volumetric flow rate (m^3/s)
x	distance (m)
μ	dynamic viscosity (Pa·s)
ρ	density (kg/m^3)
τ	shear stress (Pa)

Subscript

B	Bubble
D	Drop
FS	Free surface
G	Gas
i	Phase index
L	Liquid

Literature

- ANSYS CFX, 2013. User Manual. Ansys Inc.
- Azzopardi, B.J., Whalley, P.B., 1980, "Artificial Waves in Annular Two-Phase Flow," *Basic Mechanisms in Two-Phase Flow and Heat-Transfer*, pp. 1-8.
- Bieberle, A., Nehring, H., Berger, R., Arlit, M., Härting, H.-U., Schubert, M., Hampel, U. 2013, Compact high-resolution gamma-ray computed tomography system for multiphase flow studies. *Rev. Sci. Instrum.*, 84, 033106.
- Brocchini, M., Peregrine, D. H. 2001, The dynamics of strong turbulence at free surfaces. Part1. Description, *J. Fluid Mech.*, 449, pp. 225-254.
- Butterworth D. and Pulling DJ. 1972, Air-water annular flow in a horizontal tube, *Prog. Heat Mass Transfer* 6:235-251
- Cousins, L.B., Hewitt, G.F., 1968, Liquid Phase Mass Transfer in Annular Two-Phase Flow: Droplet Deposition and Liquid Entrainment, UKAEA Report No. AERER5657.
- Darling, R. S. and McManus, H. N. 1968, Flow Pattern in Circular Ducts with Circumferential Variation of Roughness: a Two-Phase Flow Analogy, *Dev. Mech.*, 5, 153-163
- Flores, A.G., K.E. Crowe, P. Griffith 1995, Gas-phase secondary flow in horizontal, stratified and annular two-phase flow, *International Journal of Multiphase Flow*, Volume 21, Issue 2, pp. 207-221.
- Fukano T, Ousaka A. 1989, Prediction of the circumferential distribution of film thickness in horizontal and near-horizontal gas-liquid annular flows. *Int J Multiph Flow* 15:403–419
- Hänsch, S.; Lucas, D.; Krepper, E.; Höhne, T. 2012, A multi-field two-fluid concept for transitions between different scales of interfacial structures, *International Journal of Multiphase Flow* 47, pp. 171-182
- Hewitt GF, Jayanti S, Hope CB. 1990, Structure of thin liquid films in gas-liquid horizontal flow. *Int J Multiph Flow* 16:951–957
- Hewitt, G. F., and Hall-Taylor, N.S. 1970, *Annular Two-phase Flow*, pp. 136-148. Pergamon Press, N. Y.
- Höhne, T. and Mehlhoop, J. P. 2014, Validation of closure models for interfacial drag and turbulence in numerical simulations of horizontal stratified gas–liquid flows, *International Journal of Multiphase Flow*, Volume 62, pp. 1-16
- Höhne, T., Deendarlianto, Lucas, D. 2011, Numerical simulations of counter-current two-phase flow experiments in a PWR hot leg model using an interfacial area density model. *Int. J. Heat Fluid Flow* 32, 1047–1056.
- Höhne, T., Vallée, C. 2010, Experiments and numerical simulations of horizontal two phase flow regimes using an interfacial area density model, *The Journal of Computational Multiphase Flows* 2(2010)3, 131-143.
- Ishii, M., and M. A. Grolmes. 1975, Inception criteria for droplet entrainment in two-phase concurrent film flow, *AIChE Journal*, Vol. 21, No. 2, p. 308-318.
- Ishii, M., Hibiki, T. 2006, *Thermo-fluid Dynamics of Two-phase Flow*. Springer-Verlag.
- Jayanti S, Hewitt GF, White SP. 1990, Time-dependent behaviour of the liquid film in horizontal annular flow. *Int J Multiph Flow* 16:1097–1116
- Kataoka, I., Ishii, M. 1982, Mechanism and Correlation of Droplet Entrainment and Deposition in Annular Two-phase Flow. NUREGE/CR-283J, ANL-82-44.
- Kopplin CR. 2004, Local liquid velocity measurements in horizontal, annular two-phase flow. PhD Thesis. University of Wisconsin- Madison
- Ma, J., Oberai, A., Drew, D., Jr, R. L., Hyman, M. 2011, A comprehensive sub-grid air entrainment model for rans modeling of free surface bubbly flows. *JCMF* 3, 41-56.
- Moraga, F., Carrica, P., Drew, D., Lahey Jr., R. 2008, A sub-grid air entrainment model for breaking bow waves and naval surface ships. *Computers & Fluids* 37, 281298.
- Newitt, D. M., N. Dombrowski, and F. H. Knelman. 1954, Liquid Entrainment: I, The Mechanism of Drop Formation from Gas or Vapor Bubbles, *Trans. Inst. Chem. Eng.*, 32, 244.

- Paras SV, Karabelas AJ. 1991, Properties of the liquid layer in horizontal annular flow. *Int J Multiph Flow* 17:439–454
- Russell, T.W.F., Lamb D.E. 1965, Flow Mechanism of Two-Phase Annular Flow, *The Canadian Journal of Chemical Engineering*, pp. 237-245.
- Schubring D, Shedd TA. 2008, Wave behavior in horizontal annular air-water flow. *Int J Multiph Flow* 34:636–646
- Shedd TA, Newell TA. 1998, Automated optical liquid film thickness measurement method. *Rev Sci Instr* 69:4205–4213
- Stevanovic V. and Studovic M. 1995, A simple model for vertical annular and horizontal stratified two-phase flows with liquid entrainment and phase transitions: one-dimensional steady state conditions, *Nuclear Engineering and Design*, Vol. 154, pp. 357-379.
- Taitel, Y., and Dukler, A. E. 1976, A model for predicting flow regime transitions in horizontal and near horizontal gas-liquid flow. *AIChE J.* 22, 47-55.
- Westende, J.M.C. van 't , R.J. Belt, L.M. Portela, R.F. Mudde, R.V.A. Oliemans 2007, Effect of secondary flow on droplet distribution and deposition in horizontal annular pipe flow, *International Journal of Multiphase Flow*, Volume 33, Issue 1, pp. 67-85
- Woodmansee, D.E., Hanratty, T.J. 1969, Mechanism for the Removal from a Liquid Surface by a Parallel Air Flow, *Chemical Engineering Science*, 24, pp. 299-307.
- Yegorov, Y., Menter, F. 2004, Contact condensation in stratified steam-water flow, *EVOL-ECORA –D* 07.